

GT2011-45(*) *

DETAILED HEAT TRANSFER DISTRIBUTIONS AND PRESSURE DROP MEASUREMENTS FOR A ROTATING PARALLELOGRAM CHANNEL WITH RADially OUTWARD FLOW

S.W. Chang¹, T.-M. Liou², T.-H. Lee³

¹ Corresponding author
 Professor,
 Thermal Fluids Laboratory,
 National Kaohsiung Marine University,
 No. 142, Haijhuang Road, Nanzih District,
 Kaohsiung City 81143, Taiwan, R.O.C.
 Email: swchang@mail.nkmu.edu.tw

² Professor,
 Department of Power Mechanical Engineering,
 National Tsing Hua University,
 Hsinchu, Taiwan, R.O.C.
³ Research student,
 Department of Marine Engineering,
 National Kaohsiung Marine University.

ABSTRACT

This experimental study examines the pressure drop coefficients (f) and the detailed Nusselt numbers (Nu) distributions over two opposite leading and trailing walls roughened by 45° ribs for a rotating parallelogram channel with radially outward flow. For the first time the isolated effects of Reynolds (Re), rotation (Ro) and buoyancy (Bu) numbers on local and area averaged Nusselt numbers (Nu and \overline{Nu}) measured from the infrared thermography method were successfully examined at the parametric conditions of $5000 \leq Re \leq 15000$, $0 \leq Ro \leq 0.3$ and $0.001 \leq Bu \leq 0.23$ for the single-pass parallelogram channel. A set of selected heat transfer data illustrates the Coriolis and rotating-buoyancy effects on the detailed Nu distributions and the area-averaged heat transfer performances of the rotating parallelogram channel. With the consideration of the f data generated at the isothermal conditions, the thermal performance factors (η) for this radially rotating channel were evaluated. The Nusselt numbers obtained from the leading and trailing walls of the rotating test channel fall in the respective ranges of 0.78-1.34 and 1.09-1.38 times of the stationary levels; while the η factors are in the range of 0.979-1.575 for the present test conditions.

Keywords: Rotating Parallelogram Channel, Turbine Rotor Blade Cooling.

NOMENCLATURE

English symbols

Bu Buoyancy number $= Ro^2(\Delta\rho/\rho)(r/d)$
 C_p Constant specific heat ($\text{Jkg}^{-1}\text{K}^{-1}$)
 d Hydraulic diameter of the test channel (m)
 e Rib height (m)
 f Pressure drop coefficient $= [\Delta P / (0.5\rho W_m^2)] / (d/4L)$
 f_∞ Blasius equation for turbulent flow $= 0.079Re^{-0.25}$
 H Channel height (m)
 k_f Thermal conductivity of fluid ($\text{Wm}^{-1}\text{K}^{-1}$)
 l Rib land (m)
 L Channel length (m)
 \overline{Nu} Area-averaged Nu over rotating channel

Nu Local Nusselt number of rotating channel
 Nu_0 Local Nusselt number of stationary channel
 Nu_∞ Nusselt number value evaluated from Dittus-Boelter correlation
 P Rib pitch (m)
 Pr Prandtl number $= \mu C_p / k_f$
 q Convective heat flux (Wm^{-2})
 R Dimensionless rotating radius at mid-span of test duct from rotating axis (r/d)
 r Rotating radius at mid-span of test duct (m)
 Re Reynolds number $= \rho W_m d / \mu$
 Ro Rotation number $= \Omega d / W_m$
 T_b Fluid bulk temperature (K)
 T_w Wall temperature (K)
 T_∞ Ambient temperature (K)
 W Channel width (m)
 W_m Mean flow velocity (ms^{-1})
 x, y Axial and spanwise coordinates (m)
 X, Y Dimensionless coordinates ($= x/d, y/d$)

Greek Symbols

α Attack angle of ribs ($= 45^\circ$)
 β Thermal expansion coefficient of fluid (K^{-1})
 η Thermal performance factor $= (\overline{Nu} / Nu_\infty) / (f/f_\infty)^{1/3}$
 θ Included angle of the parallelogram ($= 60^\circ$)
 ρ Density of fluid (kgm^{-3})
 μ Fluid dynamic viscosity ($\text{kgm}^{-1}\text{s}^{-1}$)
 Ω Rotational speed of test duct (rads^{-1})

Subscripts

0 Refers to non-rotating situation

INTRODUCTION

The life span of a gas turbine rotor blade depends on its material temperatures and therefore the cooling technology deployed. In a modern gas turbine rotor blade, the airflow extracted from the compressor is channeled through the internal coolant passages. Various Heat Transfer Enhancement (HTE) devices are fitted in these internal coolant channels to promote their cooling effectiveness. These HTE performances are subject to the rotation induced influences, namely the Coriolis and rotating buoyancy effects. There have been

industrial and academic interests in heat transfer studies for rotating channels with internal cooling applications to gas turbine rotor blade [1-23]. With a rotating channel, the Coriolis force drives the cooler fluid toward the unstable wall where the flow is un-stabilized relative to the opposite stabilized wall. The periphery heat transfer variations with the Nu decay from the unstable to the stable walls are accordingly generated by the Coriolis force effect in a rotating channel. The Nusselt numbers on the unstable and stable walls are respectively increased and decreased from the stationary references when the rotation number increases. As the centrifugal acceleration is significantly large in an internal coolant channel of a turbine rotor blade, the buoyancy interaction can considerably affect the heat transfer performance. With radially outward and inward flows, the analogies of rotating buoyancy effects to the mixed convection for the counter- and parallel-flow conditions were reported in [7]. Among these previous studies [1-23], Johnson et al. [7] firstly generated the Nusselt number data from the rotating ribbed channel at high rotating numbers up to 0.45. For the stable wall of the rotating serpentine passage, the heat transfer recovery from the Ro driven heat transfer impairing trend was firstly reported. The dimensionless forms which respectively characterized the inertial, Coriolis and rotating-buoyancy effects on heat transfer were confirmed as Re , Ro and Bu by this study [7]. The later works of Morris group [9] has demonstrated that the Reynolds number effect on rotational Nusselt number can be isolated from the Ro and Bu impacts by scaling the rotational Nusselt numbers with those obtained from the stationary channel. A procedure for parametric analysis which isolates Re , Ro and Bu effects is accordingly devised, leading to the generation of the physically consistent heat transfer correlations. A large number of rotating single- and twin-pass channels with various shapes and channel orientations was systematically examined by Han group [1,6,12,14,15]. Their consistent efforts enlightened the various Coriolis effects developed in the square, rectangular and triangular ribbed channels with the complex flow interactions between the rib-induced and Coriolis flows illustrated.

Following the blade profile from its nose, mid-chord to trailing edge, the internal coolant channels vary from the trapezoidal, rectangular/square/parallelogram to nearly triangular shapes. Along with the chord-wise variations in channel orientation and sectional shape, the periphery which confines the Coriolis secondary flows for each rotating channel is accordingly varied, leading to various rotational effects on heat transfer properties [1-23]. Different HTE performances reported for the rotating channels of various cross-sectional shapes [1-21] mainly reflect the various structures of Coriolis secondary flows. In this respect, the comparative heat transfer differences between the rotating channels with different channel orientations [1-2,6] and different sectional shapes [3-4] as well as the heat transfer performances in the triangular [3,5-6], square [1,7-10,20], rectangular [2,11-16] and trapezoidal [17-18] single-, twin- or triple-pass channels are examined. For the rotating rectangular

ribbed channels, the considerable effects of the channel aspect ratio (AR), which is defined as the channel width-to-height ratio, on the fluid flow and heat transfer were reported through their impacts on the strength of the Coriolis secondary flow and the area fraction of the ribbed surface [12-14,16]. The numerical work [13] concluded the more intense Coriolis secondary flow in the channel with a smaller AR but a more intense rib-induced secondary flow in the channel with a larger AR [13]. Heat transfer enhancements on the unstable ribbed walls of the rotating rectangular channel decreased systematically as AR increased. As a general trend of the rotational influences on heat transfer at high Ro ($Ro > 0.4$) [2,7,10,15-18], the Nu on the unstable wall are consistently improved from the zero-rotation references as Ro increases; while the Nu on the stable wall are initially reduced from the zero-rotation references but recovered as Ro exceeds the critical value (Ro_{cr}). For the rectangular ribbed channels with $0 \leq Ro \leq 2$, the critical Ro_{cr} were 0.1, 0.1 and 0.3 for the test channels of AR=1, 2, 4 respectively [16]. With triangular [5-6] and trapezoidal [17-18] rotating channels, their narrow sharp apical end significantly confine the Coriolis secondary flow. The typical pairing pattern of Coriolis secondary flows can be diminished in the triangular rotating ribbed channel and transformed into the single cell pattern [6], leading to different Ro effects from those in the rectangular channels [2, 11-16,19]. Although the parallelogram appears as a typical shape of the internal coolant channel inside a gas turbine rotor blade, the relevant heat transfer study is very rare. Peter [22] performed the heat transfer measurements for the rotating parallelogram ribbed channel and reported three distinct flow regions, namely the developing, intermittent and periodically developed flow regions, along this channel at both stationary and rotating conditions. Relative to the similar rectangular channel of AR=2 [23], \overline{Nu} is elevated by the twisted near-wall flows along the obtuse corner of the rotating parallelogram channel.

In addition to the search of various heat transfer performances for the simulated coolant channels in a gas turbine rotor blade at the test conditions emulating the realistic engine conditions at high Ro [2,7,9,15-18], another research pursuit is directed to acquire the full field Nu data with the rotating buoyancy effect examined. As discussed in [21], the fast progress of this research development has been prohibited by the capability to generate the full Nu scans at prescribed buoyancy levels when the methods involving the naphthalene sublimation or the liquid crystal thermal images were used. The pressing needs to acquire the full Nu scans involving the buoyancy effect, together with the attempt to examine the various HTE performances in the rotating channels, have motivated this research group to devise the steady state infrared thermography method for measuring the full field Nu over the rotating ribbed and wavy channels [20-21]. Due to the lack of the full Nu data for the rotating parallelogram channel, this experimental study is formulated to examine the Coriolis and rotating buoyancy effects on the detailed Nu distributions over the leading and trailing walls of a rotating parallelogram channel with two opposite walls roughened by 45° in-line ribs.

The rotating parallelogram channel is in common use for gas turbine rotor blade cooling; while no full field Nu data is currently available. The surface temperatures (T_w) over the two opposite leading and trailing ribbed walls of the rotating parallelogram channel with radial outward flow are measured by the infrared camera which acquires the full-field T_w scans at the prescribed buoyancy levels. The pressure drop coefficients measured at various rotating test conditions are comparatively examined with the HTE ratios to determine the η factors for this rotating parallelogram channel. One of the major benefits from this experimental study is the added insight gained into the thermal physics arising from the full field Nu data involving the rotating buoyancy effect.

EXPERIMENTAL METHODS

Experimental facilities

The rotating test rig used to measure the full Nu scan is shown in Fig.1 and comprises a pair of rotating arms, the coolant and power supplies, the signal transmission devices, and a rotating platform on which the assorted test module is mounted [20-21]. The rotating arms are for securing the infrared camera (IC) and its counter-balanced weight. This rotating rig and measurement technique have been previously validated by comparing the Nu data obtained from the twin-pass radially rotating channel fitted with skewed ribs [20] to the well-known published data reported by Johnson et al. [7]. The favorable agreements between the Nu data generated by the two studies [7, 20] are obtained. The parallelogram-sectioned test module is mounted on the rotating platform with a mean rotating radius (r) of 600 mm to the mid-span of the test section. The rotor is driven by a variable-speed DC motor via a pulley system using three V belts. Two separate power slip-ring units transmit the electrical powers to the test section and the IC and the electronic micro-manometer. Another two separate sets of instrumentation slip rings transmit the thermocouple signals measuring the fluid entry and exit temperatures to the Fluke Net-Daq 2640A data logger, and T_w scans detected by IC respectively. The signals from the micro-manometer for measuring the pressure drops through the rotating test channel are also transmitted through the instrumentation slip ring for IC signals. Rotor speed is measured by the optical pick-up and encoder unit from the shaft. The complete rotor assembly is dynamically balanced by the counter weights. The rotating speeds of the test channel, which is limited by the maximum sustainable acceleration of IC, are in the range of 0-110 rev/min. The dry and cool pressurized airflow is channeled through the rotary seal, the shaft bore, the test channel and the exhaust valve at the exit of the test module. The airflow pressure in the test section is controlled by adjusting the exhaust valve. The range of the airflow absolute pressures in the test channel is 1.1-1.4 bar. Adjustments of the rotor speed and the test pressure enable both Re and Ro to be controlled simultaneously at the target values. Please refer to our previous studies [20-21] for more details.

The parallelogram test channel with two opposite leading and trailing walls roughened by in-line skew ribs, as well as the

layout of the test section with the IC position relative to the test rig are depicted by Fig. 1. The width (W) of 60mm, height (H) of 30mm and the included angle (θ) of 30 degrees for the parallelogram test channel give rise to the channel width-to-height ratio (aspect ratio, AR) of 2 and the channel hydraulic diameter (d) of 40mm. The two opposite rib-roughened leading and trailing walls are heated with the basically uniform heat fluxes. Active heating length of each heated wall (L) is 340mm, giving the L/d ratio of 8.5. The test parallelogram channel is rotated orthogonally to the axis of rotation. Fig. 1 indicates the leading and trailing walls relative to the direction of rotation and the x - y coordinate system adopted by this study.

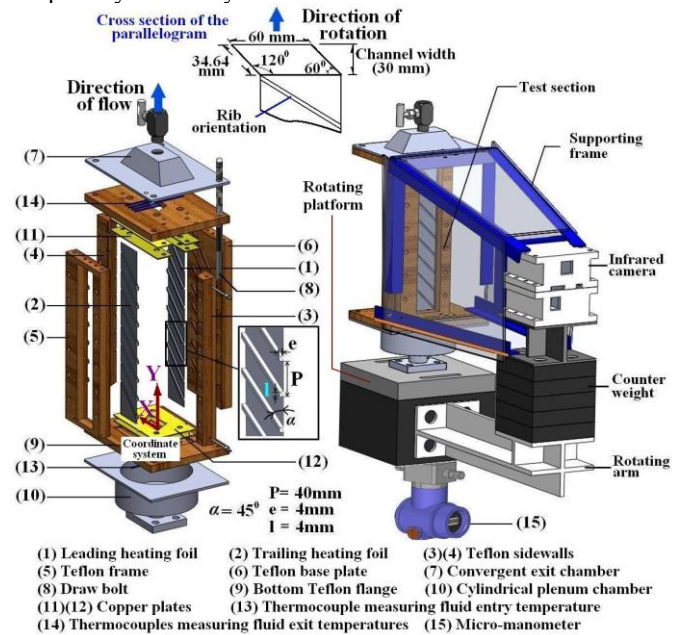


Fig. 1 Parallelogram test module.

The two opposite leading and trailing ribbed walls (1)(2) are made of two continuous 0.1mm thick stainless steel foils to forge into the required geometries. The 45° ribs are arranged in the in-line manner over the leading and trailing walls. As indicated by Fig. 1, the rib pitch-to-height ($P/e=40\text{mm}/4\text{mm}$), rib land-to-height ($l/e=4\text{mm}/4\text{mm}$) and the rib-height to channel-height ($e/H=4\text{mm}/30\text{mm}$) ratios are 10, 1 and 0.13 respectively. The uniform heat flux is generated by the joule heat when the electrical current flows through each of the two rib roughened stainless steel foils (1)(2). The ribbed stainless steel heating foil (1) over which the detailed T_w are scanned is sandwiched between the two Teflon side walls (3)(4) and the Teflon frame (5) by 12 axial bolts, Fig. 1. Another ribbed stainless steel heating foil (2) is attached on the Teflon base plate (6), which consolidates with the two Teflon sidewalls (3)(4) and the scanned heating foil (1) to form the parallelogram test section. As heat fluxes also dissipate from the edges of the heating foils to the Teflon frames, Teflon sidewalls and convect to the surrounding ambience from the back-surface of the heating foil (1), a portion of the supplied heat will turn into the heat loss via the conduction and convection pathways. This portion of heat loss can be approximated using the heat-loss correlation generated through the heat loss calibration tests. As indicated in Fig. 1,

the heat transfer test module is shielded with the IC so that the heat loss flux from the back surface of the scan wall can be reduced at each rotational test. The evaluation of the local convective heat flux is based on the total heating area, including all the rib surfaces, with the heat loss flux deducted from the total heat flux supplied. This will be further described in the ensuing section.

A convergent air chamber (7) is installed at the exit of the test section, on which an exhaust valve is attached. The test parallelogram channel is tightened by the axial bolts and four draw bolts (8) between the flange of the exit air chamber (7) and the bottom Teflon flange (9) connecting with the air entry plenum chamber (10) on the rotating platform. The cylindrical air chamber (10) with a cross-sectional area of 17357 mm² is filled with steel meshes, which simulates the abrupt entry condition with the cross sectional area ratio between the entry plenum chamber and the test channel of 9.64. The two axial ends of each stainless steel foil (1)(2) are sandwiched between two pairs of copper plates (11)(12) that connect with electrical cables to form the electrical heating circuit. A type K thermocouple (13) is installed at the center of the flow entry plane to measure the inlet fluid temperature. For each heat transfer test, the Re and Ro at the flow entry are constantly calculated and monitored based on the airflow rate fed into the test channel and the fluid inlet temperature detected by thermocouple (13). Eight type K thermocouples (14) are arranged with equal interval over the exit plane of the test channel to measure the fluid exit temperatures. The measured fluid bulk temperature (T_b) at the exit is obtained by averaging the readings from these eight thermocouples (14). When the differences between several successive T_w readings at the selected spots on the scanned heating surface are less than 0.3^oC, the experimentally defined steady state is assumed. The steady-state T_w scan transmitted from the IC are stored in a PC for the subsequent data processing. The calculation of local T_b along the test channel at each test condition adopts the enthalpy balance method based on the local convective heat flux and the measured fluid entry temperature. As a constant test routine, the measured and calculated exit T_b is compared during each heat transfer test run. The experimental raw data at the steady state are collected only if the differences between the calculated and measured exit T_b are less than 10%. The local T_b along the test channel are selected as the referenced fluid temperatures to evaluate local Nu and all the temperature dependent fluid properties required during the process of data reduction, such as the thermal conductivity and viscosity of the coolant. The characteristic length selected to define Re , Ro , Bu and Nu is the channel hydraulic diameter (d).

The present infrared thermal image system takes 60 frames of 239×255 matrix T_w scan in one second. The back surface of the scanned heating foil (1) is painted black to enhance the infrared emission. During the calibration tests for this infrared thermal image in the temperature range of 20–180^oC, the differences between the temperatures measured by the infrared radiometer and the thermocouples are less than 0.7^oC after adjusting the emissivity coefficient as 0.85 for this test configuration. The shield that envelops the IC and the heat transfer test module indicated in Fig. 1 can also reduce the disturbances from the background emissions and the flow

over the scanned foil (1) when the test channel is rotating. Pressure drops across the stationary and rotating test channel are individually measured at the isothermal conditions using the digital micro-manometer (15) with the precision of 0.01 mm-H₂O. The micro-manometer (15) is fixed on the opposite side of the rotating platform and connected with two pressure taps installed at the flow entrance and exit of the test section. The heat transfer and pressure drop performances, as well as the thermal performance factors, acquired from the stationary and rotating tests are comparatively examined to disclose the influences of rotation on the thermal performances of the parallelogram ribbed test channel.

Experimental program and data processing

Heat transfer tests were initially performed at the stationary conditions with five Re of 5000, 7500, 10000, 12500, and 15000. For each Re , a series of rotating tests at the parametric conditions summarized in Table 1 were undertaken. With rotating heat transfer tests, the T_w distributions over the leading wall were initially measured after which the trailing-wall T_w scans were performed by reversing the direction of rotation.

Table 1 Parametric test conditions

Parameter	Range
Reynolds number [Re]	5000, 7500, 10000, 12500, 15000
Rotation number [Ro]	0 – 0.3
Buoyancy number [$Bu = \beta(T_w - T_b)Ro^2(R/d)$]	0.001 – 0.23
Density ratio [$\Delta\rho/\rho = \beta(T_w - T_b)$]	0.0063 – 0.195
Tested Ro for each Re	
Re	Ro
500	0.05, 0.075, 0.1, 0.15, 0.2, 0.25, 0.3
75000	0.05, 0.075, 0.1, 0.15, 0.2
10000	0.05, 0.075, 0.1, 0.15
12500, 15000	0.05, 0.075, 0.1

At each Re - Ro tested, four ascending heater powers that raised the highest T_w on the scanned wall to 75, 100, 120, and 140^oC were used to elevate the rotating buoyancy level (Bu) by increasing the density ratio [$\beta(T_w - T_b)$] at the fixed Ro . As the test coolant (dry air) follows the ideal gas law, the density ratio ($\Delta\rho/\rho$) is determined as $\beta(T_w - T_b)$. Clearly, this $\Delta\rho/\rho$ value for determining $Bu = \beta(T_w - T_b)Ro^2(r/d)$ appears as a local value since $T_w - T_b$ varies with x and y . It is thus impractical to control Bu at a pre-defined targeting value for each heat transfer test. The nominal Bu for each set of rotational heat transfer result was obtained afterward by averaging all the local Bu obtained from the scanned wall. However, local $\beta(T_w - T_b)$ and Bu were accordingly adjusted when the heater power was varied. The isolated Bu effect on heat transfer at the tested Re and Ro could be readily realized by comparing the four sets of Nu scans obtained at different Bu . As the adjustment of heater power changed local T_b that affected the fluid properties such as viscosity, the airflow rate was constantly adjusted to compensate the changes of fluid properties in order to maintain Re and Ro at the targeting values with $\pm 1\%$ deviations on the flow entrance. Having completed the heat transfer tests, the pressure drop data at the isothermal

conditions for each Re and Ro tested were measured. A subsequent parametric analysis exploring the functional relationships for \overline{Nu} and f with their controlling parameters was performed. The Nu variation responding to each of the controlling dimensionless parameters (i.e. Re , Ro , and Bu) while the others remain unchanged signifies the individual impact of the varying parameter on heat transfer. The varying manners of f coefficients against Ro at each tested Re reveal the effect of Coriolis force on the pressure drops for this parallelogram channel. With T_b varying between 27.4-70.7°C, the maximum variation in Prandtl number (Pr) is about 1.4%, which is negligible. The Pr effect on Nu is not investigated.

Local Nu over the scanned ribbed wall is evaluated as $Nu = q_f d / \{k_f (T_w - T_b)\}$ in which the local convective heat flux (q_f) is calculated by subtracting the heat loss flux from the total heat flux supplied. Heat-loss characteristics are determined by conducting a series of heat-loss calibration tests at five rotating speeds. To perform the heat loss calibration test, the test channel was blocked and filled with thermal insulation fiber. The steady state was achieved at the particular temperature level depending on the power supply and the heat loss characteristics which varied with rotating speed. The supplied heat flux was balanced with the heat loss flux (q_{loss}) at the steady state. The heat loss characteristic at each rotating speed tested is correlated by the equation of

$$q_{loss} = k_L \times (\overline{T}_w - T_\infty) \quad (1)$$

in which k_L represents the heat loss coefficient and \overline{T}_w and T_∞ are the averaged mean wall temperature and the ambient temperature respectively. \overline{T}_w was obtained by averaging the wall temperature scan detected by the IR thermal image system. When the rotational speed (Ω) increases, k_L increases accordingly. The various k_L values obtained at different rotating speeds are correlated into the Ω controlled function for the subsequent data processing. The maximum percentage of the overall heat flux lost to the ambience was about 23%. The local heat loss flux at the prescribed ($\overline{T}_w - T_\infty$) and the test rotor speed can be accordingly determined using the heat loss correlation generated. The T_w distribution over the scanned rib floor is not uniform. The convective heat flux (q_f) is obtained by subtracting q_{loss} , which is evaluated as $k_L \times (\overline{T}_w - T_\infty)$, from the total supplied heat flux. Therefore the distributions of heat loss flux and q_f on the leading or trailing walls are not uniform. A review of the entire q_f data indicates that the maximum non-uniformity for q_f distribution is about 11%. With q_f determined, the calculation of streamwise T_b increase from the measured fluid entry temperature can be performed. The local fluid bulk temperature is determined based on the local enthalpy balance in the form of

$$q_f \times (S \times \Delta y) = \dot{m} C_p dT_b \quad (2)$$

where S is the heating perimeter at y location and \dot{m} is the measured mass flow rate. By means of a sequential integration of the local enthalpy balance from the initial axial location y_i to the subsequent downstream location y_{i+1} , the fluid bulk temperature at y_{i+1} is approximated as

$$T_b(y_{i+1}) = T_b(y_i) + S / (\dot{m} C_p) \times q_f(y_i) \times (y_{i+1} - y_i) \quad (3)$$

where S , \dot{m} , q_f and $(y_{i+1} - y_i)$ are the measured quantities. This

sequential integration process starts from the flow entry where the fluid bulk temperature is detected. The fluid properties at each streamwise section are accordingly defined using the local T_b .

The pressure drop coefficient is evaluated as the Fanning friction factors (f) using the pressure drops (ΔP) across the test duct of length L with mean flow velocity (W_m) as

$$f = [\Delta P / (0.5 \rho W_m^2)] / (d / 4L) \quad (4)$$

The references selected to assess the HTE ratios and the pressure-drop augmentations for this rotating parallelogram ribbed channel are the levels in a smooth circular tube with fully developed flow. The reference Nusselt number (Nu_∞) and friction factor (f_∞) are respectively defined as

$$Nu_\infty = 0.023 Re^{0.8} Pr^{0.4} \text{ (Dittus-Boelter correlation)} \quad (5)$$

$$f_\infty = 0.079 Re^{-0.25} \text{ (Blasius equation)} \quad (6)$$

The thermal performance factor (η) based on constant pumping power consumption at each set of tested Re and Ro is defined as

$$\eta = (\overline{Nu}_{mean} / Nu_\infty) / (f / f_\infty)^{1/3} \quad (7)$$

where the mean Nusselt number (\overline{Nu}_{mean}) is calculated as the averaged value over the leading and trailing walls.

The experimental uncertainties for Nu , f , Re , Ro and Bu are approximated [24]. The fluid temperature measurements are the major sources attributed to the experimental uncertainties for Nu , Re , Ro and Bu as all the fluid properties are temperature dependent. For f measurements, the experimental uncertainty is mainly attributed to ΔP measurements. With the prescribed precisions for the measuring devices, the percentages of error for temperature and flow measurements are reduced at the test condition with the high heater power and large flow rate. The experimental uncertainties for Nu are generally reduced for the tests at high Re and high Bu ; while the f uncertainties are reduced at high Re due to the larger ΔP . With $T_w - T_b$ in the range of 21-68.23, the maximum uncertainties for Nu , f , Re , Ro and Bu are about 9.3%, 4.6%, 4.2%, 6.5% and 7.8% respectively.

RESULTS AND DISCUSSION

Heat transfer measurements

Stationary channel

The Nusselt number data obtained at static conditions are initially examined to generate the heat transfer references for comparing with the rotational Nusselt number to reveal the influences of rotation on heat transfers over the leading and trailing ribbed walls of the parallelogram channel. Fig. 2 depicts the full field T_w , Nu_0 , and axial centerline Nu_0 variation on the rib floor of the static test channel at $Re = 15000$ and $q_f = 2912.5$ (Wm^{-2}). They are typical of the stationary heat transfer results obtained at all Re tested. In the static parallelogram ribbed channel, the near-wall flows together with the sectional flows tripped by the 45° ribs generate the rib-wise T_w increases over the rib floor from the obtuse toward the acute edges, as shown in Fig. 2(a). The attendant rib-wise obtuse-to-acute Nusselt number

declinations on the rib floor are clearly seen in Fig. 2(b). The accelerated and separated flows caused by the abrupt blockage of the protruding square rib produce the low wall temperature and high Nusselt number bands along the top face of each 45° rib. Additionally, the wall temperature and Nusselt number imprints typified by Figs. 2(a)-2(b) clearly show the skewed trace of the shedding vortex which is triggered at the obtuse root behind each 45° rib. This shedding vortex behind each 45° rib plays the dominant HTE role in the region between two successive 45° ribs by generating a midway skewed high Nusselt number stripe as seen in Fig. 2(b). Noticeably, the trace of such shedding vortex behind each 45° rib is already evident at the first rib in Fig. 2(a). Moreover, the trajectories of these midway low wall temperature and high Nusselt number stripes coincide with the flow path of the shedding vortex behind each angled rib [8].

Although the typical Nusselt number variations over the rib floor in the present static parallelogram ribbed channel follow the general trends reported for the square/rectangular ribbed channels [1,7-16], the subtle differences in Nusselt number distributions between the square, rectangular and parallelogram ribbed channels remain. In the square ribbed channel, the lengths of the shedding vortex behind each angle rib [8] and the midway skewed high Nusselt number stripe [20] proceed along most of the rib length. But the skewed midway low wall temperature and high Nusselt number stripes seen in Figs. 2(a)-2(b) for this parallelogram ribbed channel are wider and shorter than those developed in the similar square ribbed channels [8,20]. This indicates the thermal and momentum diffusions are more rapid in the parallelogram ribbed channels than in the rectangular counterparts. This observation provides the rationale for the previously reported higher HTE impacts attained by the parallelogram ribbed channels than by the rectangular ones [22].

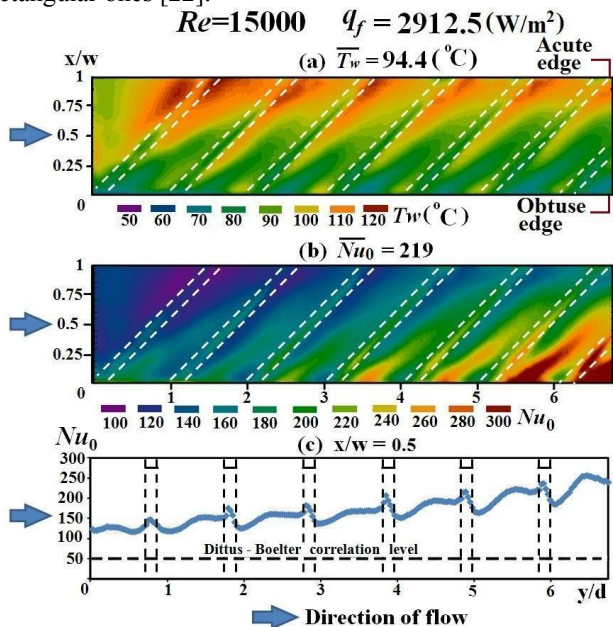


Fig. 2 Full field (a) T_w , (b) Nu_0 , and (c) axial centerline Nu_0 variation over rib floor at $q_f = 2912.5$ (Wm^{-2}).

While the typical boundary layer development in a channel increases the streamwise thermal resistance, the HTE

mechanisms tripped by the 45° ribs keep growing from the flow entrance toward the so-called periodic developed flow region. The competitive influences between the growing boundary layer thickness and the rib-triggered HTE mechanisms generate the particular axial Nusselt number variation seen in Fig. 2(c). As indicated by Fig. 2(c), the net result of these two competitive heat transfer mechanisms produces the overall centerline Nusselt number increase in the present parallelogram ribbed channel. Such axially rising Nusselt number trend along the centerline of the rib floor indicates that the dominant heat transfer physics in the developing flow region for this parallelogram ribbed channel is the rib induced flow phenomenon. It is interesting to note that the periodic developed flow regions for the square or rectangular ribbed channels are usually observed after the bulk airflow traverses about five pairs of ribs [9-10,16,20,23]. But the axial Nusselt number increase shown by Fig. 2(c) suggests that the flow in this parallelogram ribbed channel remains developing after the 7th rib. Even the streamwise growths of the rib-top Nusselt number peaks and the midway Nusselt number ripples are clearly visible in Fig. 2(c). The developing length for the rib induced flows in the parallelogram channel with the slanted cross section is extended from those in the square or rectangular ribbed channels. The area-averaged Nusselt number (\bar{Nu}_0 or \bar{Nu}) is obtained by averaging all the scanned Nusselt numbers over the entire stationary or rotating rib floor. Comparing Fig. 2(c) with the Dittus-Boelter Nusselt number (Nu_{∞}) level, the HTE impact is assured. The Nusselt number ratio (\bar{Nu}_0/Nu_{∞}) for this parallelogram ribbed channel reaches 4.3 at $Re=15000$, which is higher than the similar rectangular ribbed channel as compared in [22].

As for the validation, Fig. 3 compares the area-averaged Nusselt number (\bar{Nu}_0) obtained at $Re = 5000, 7500, 10000, 12500, 15000$ for the present stationary case with the local Nusselt numbers detected at the rib and mid-rib locations over the periodically developed flow region in a similar parallelogram channel [22]. The heat transfer data in [22] were generated with wall temperatures detected by the thermocouples embedded at the rib and mid-rib locations along the channel centerline. The two fitted Nusselt number curves [22] for the rib and mid-rib locations featured the higher and lower Nusselt number bonds for the set of experimental data reported in [22]. The present Nusselt numbers fall between the two Nusselt number correlation curves [22] in Fig. 3. For the present stationary test channel, there is no appreciable heat transfer difference between the test results acquired at four different heating levels for each Re examined. The buoyancy parameter is exclusive from \bar{Nu}_0 correlation. Justified by the Re -driven ascending \bar{Nu}_0 trend in Fig. 3 and the limiting condition of $\bar{Nu}_0 \rightarrow 0$ as $Re \rightarrow 0$, the present \bar{Nu}_0 is correlated as $\bar{Nu}_0 = 0.56 \times Re^{0.59}$. This \bar{Nu}_0 correlation is used to evaluate the stationary heat transfer references against which \bar{Nu} is normalized to assess the influences of Ro and Bu on \bar{Nu}/\bar{Nu}_0 .

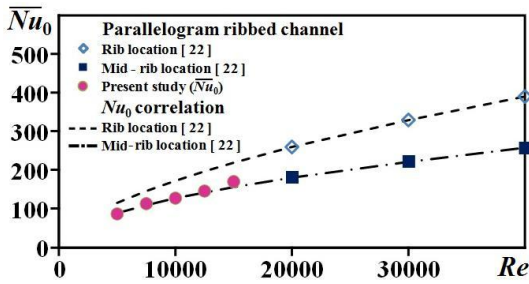


Fig. 3 A comparison of \bar{Nu}_0 versus Re

Rotating channel (Ro effect)

Fig. 4 comparatively examines the detailed Nusselt number distributions over (a) leading and (b) trailing ribbed walls of the rotating parallelogram channel at $Re=5000$, $Ro=0.3$, $Bu=0.14$ (leading) and 0.15 (trailing). Fig. 4(c) depicts the stationary Nu_0 scan at $Re=5000$. Fig. 4(d) compares the axial centerline leading and trailing Nu and Nu_0 profiles collected from Figs. 4 (a)-4(c).

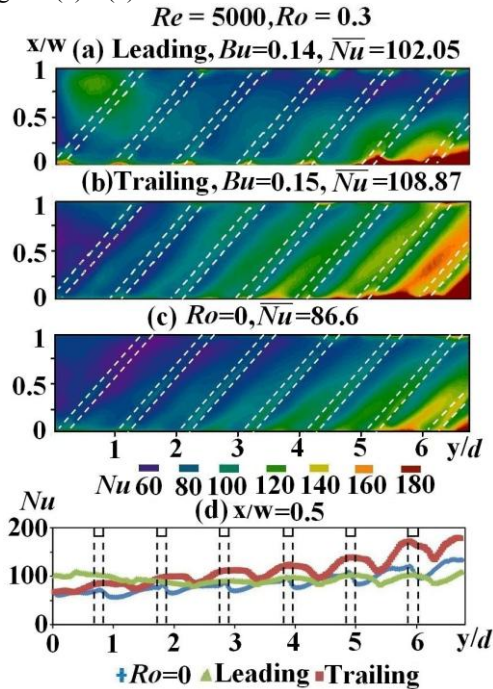


Fig. 4 Detailed Nu distributions of (a) leading ($Bu=0.14$) and (b) trailing ($Bu=0.15$) rotating wall at $Re=5000$ and $Ro=0.3$, (c) Nu_0 scan at $Re=5000$, and (d) axial centerline leading and trailing Nu profiles and Nu_0 variation collected from (a)-(c).

Over the leading and trailing rib floors, the regional high Nusselt number peaks still develop on the top faces of these 45° ribs as shown in Figs. 4(a) and 4(b). The mid-way skewed high Nusselt number stripe on the trailing wall in Fig. 4(b) generally follows the Nu_0 imprints between two successive 45° ribs in Fig. 4(c). The shedding vortex from obtuse root behind each 45° rib is still the dominant mid-way HTE mechanism over the rotating trailing rib floor. But a low Nusselt number band with a bandwidth of about one rib land attaches immediately behind each 45° ribs on the rotating trailing wall. While the characteristic pattern of the Nusselt number distributions on the rotating trailing wall follows the static result, the Nusselt number distributions over the rotating

leading wall undergo considerable modifications from the Nu_0 patterns as revealed by the comparison between Figs. 4(a) and 4(c). The most significant Nu modification from the static Nu_0 distribution on the rotating leading wall is the development of a haloed high Nusselt number zone aside the acute edge in front of the first 45° rib on the upper left corner of Fig. 4(a). Acting by the Coriolis force and the flow twist at the immediate flow entrance after the airflow enters the slanted cross section (parallelogram), a corner vortex is likely to be triggered near the edge of $x/w=1$, $y/d=0$ to surge the cold coolant toward the leading wall before hitting the first 45° rib. This corner vortex is soon disrupted after it traverses the first 45° rib on the leading wall and consequently affects the development the shedding vortex at the obtuse root behind the 45° rib on the rotating leading wall. In this regard, the Nu trace reflecting the shedding vortex behind each 45° rib on the rotating leading wall is diminished over the first three ribs; but recovered in a form of highly diffused vortical flow between two adjoining ribs after the fourth rib (Fig. 4(a)). In contrast to the low Nu band behind each 45° rib on the trailing wall depicted by Fig. 4(b), there is no clear Nusselt number valley behind each 45° rib on the leading wall as shown in Fig. 4(a). Unlike the rotating parallelogram ribbed channel, the distributing Nusselt number patterns over the two opposite leading and trailing walls of the rotating rectangular or square ribbed channels are generally similar. The differential Ro effects on Nusselt number distributions between leading and trailing walls in a rotating parallelogram ribbed channel are amplified by the slanted cross section. Due to the presence of the haloed high Nusselt number zone in front of the first 45° rib on the leading wall in the rotating parallelogram channel, the axial centerline leading Nusselt number over the first two ribs are higher than the trailing and the stationary heat transfer levels (Fig. 4(d)). After the airflow traversing 2nd rib, the Nusselt numbers along trailing centerline become consistently higher than the stationary references and the leading counterparts. Nevertheless, as demonstrated later, the $Ro=0.3$ has well exceeded the critical Ro_{cr} above which the leading Nusselt number starts increasing as Ro increases. Therefore the leading centerline Nu and \bar{Nu} are higher than the stationary counterparts as compared in Fig. 4.

The Ro effect on \bar{Nu} is parametrically examined by plotting \bar{Nu} against Ro at each tested Re over (a) leading and (b) trailing ribbed walls in Fig. 5. As well as a reconfirmation for the typical Ro effect on heat transfer, the leading \bar{Nu} is initially reduced from the \bar{Nu}_0 references as Ro increases; but recovers after Ro exceeds the critical value (Ro_{cr}) of 0.15 for this rotating parallelogram ribbed channel, Fig. 5(a). The trailing \bar{Nu} keeps increasing as Ro increases and is consistently higher than the \bar{Nu}_0 references and the leading counterparts. The Re driven upward shifts of \bar{Nu} data series are clearly seen in Figs. 5(a) and 5(b). At each fixed Ro , the Bu driven upward data trend is consistently found at each tested Re , Figs. 5(a) and 5(b). However, after normalizing \bar{Nu} by \bar{Nu}_0 , all the \bar{Nu}/\bar{Nu}_0 obtained with different Re but at a fixed Ro are converged, which has led to the two Ro -driven \bar{Nu}/\bar{Nu}_0 trends for the leading and trailing walls as indicated in Fig. 5(c) and 5(d) respectively. In Fig. 5(c) or 5(d) at

$Ro=0.05$ for either leading or trailing wall, there are twenty $\overline{Nu}/\overline{Nu}_0$ ratios obtained at five Re with four Bu . Therefore the $\overline{Nu}/\overline{Nu}_0$ data band at each Ro shown by Fig. 5(c) deems to be the buoyancy impact. The isolation of Re effect for the rotational influences on heat transfer by presenting the heat transfer data in terms of $\overline{Nu}/\overline{Nu}_0$ is confirmed. The Re exponent in \overline{Nu}_0 correlation remains as it was.

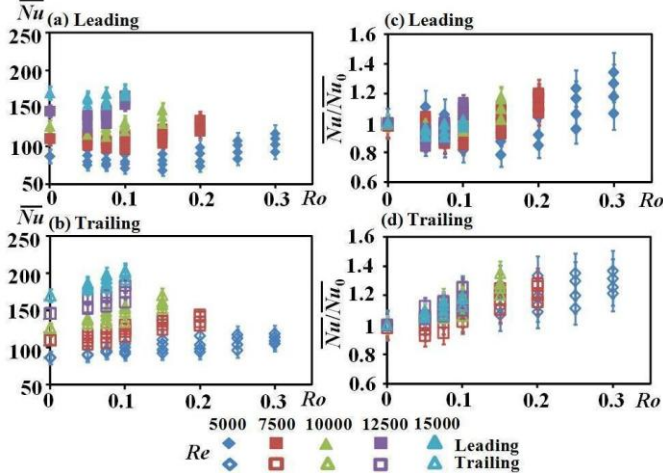


Fig. 5 Variations of \overline{Nu} against Ro at each tested Re over (a) leading (b) trailing ribbed walls (c)(d) $\overline{Nu}/\overline{Nu}_0$ versus Ro at all Re and Bu tested on leading and trailing walls.

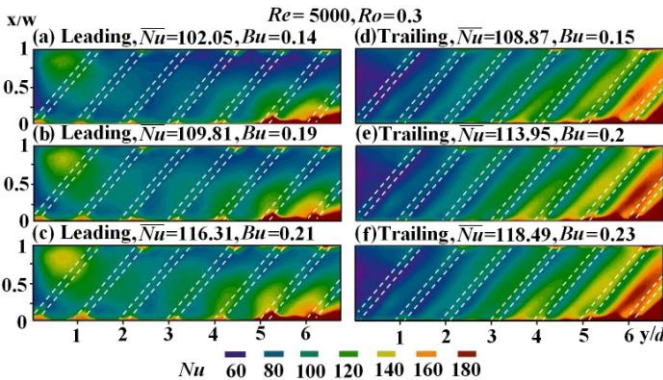


Fig. 6 Detailed Nu distributions with three ascending Bu over leading (a) (b) (c) and trailing (d) (e) (f) rib floors.

Rotating channel (Bu effect)

Figure 6 depicts the detailed Nu distributions at $Re=5000$ and $Ro=0.3$ with three ascending Bu levels over leading (a) (b) (c) and trailing (d) (e) (f) rib floors. At the fixed Ro , the increase of nominal Bu over each these rotating rib floors is caused by raising the heater power to increase the density ratio ($\Delta\rho/\rho$) evaluated as $\beta(T_w-T_b)$. The Bu increase produces the attendant \overline{Nu} increase over the leading and trailing rib floors without altering their characteristic patterns of Nu distributions, Fig. 6. On the leading rib floor, the high Nu region tripped by the corner vortex at the entry upper left corner of the rotating parallelogram ribbed channel is systematically enlarged as Bu increases, Figs. 6 (a)-6(c). Another comparative result caused by increasing Bu seen in Figs. 6 (a)-6(c) and Figs. 6 (d)-6(f) is the extended high Nusselt numbers over the mid-way regions between two adjacent skew ribs on leading and trailing rib floors. The corner vortex triggered at the entry upper left corner on the leading rib floor as well as the shedding vortex

behind each skewed rib over both leading and trailing rib floors are enhanced by increasing Bu at the fixed Re and Ro . Such vortex enrichment serves as the main HTE mechanism for the improving Bu effect on \overline{Nu} over the rotating leading and trailing ribbed walls in the rotating parallelogram ribbed channel.

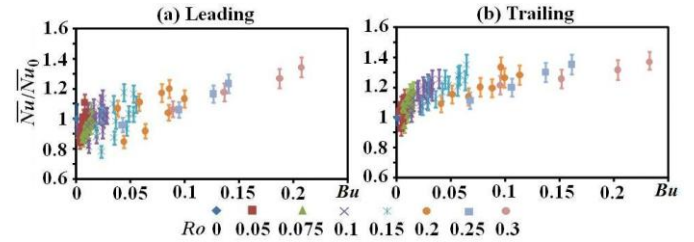


Fig. 7 Variations of $\overline{Nu}/\overline{Nu}_0$ against Bu at fixed Ro over (a) Leading and (b) trailing rib floors.

The Bu effects on \overline{Nu} over the rotating (a) leading and (b) trailing rib floors are examined by plotting $\overline{Nu}/\overline{Nu}_0$ against Bu at the fixed Ro in Fig. 7. The entire Nusselt number ratios ($\overline{Nu}/\overline{Nu}_0$) obtained from the leading and trailing rib floors at the present rotating test conditions covering the developing flow region fall in the respective ranges of 0.78-1.34 and 1.09-1.38. The leading and trailing Nusselt number ratios ($\overline{Nu}/\overline{Nu}_0$) are in the ranges of 2.97-5.05 and 3.52-5.65 respectively. As indicated in Table 1, there are various Re at each fixed Ro . Therefore each Bu -driven $\overline{Nu}/\overline{Nu}_0$ series obtained at a fixed Ro seen in Fig. 7 constitutes several different tested Re . These Bu -driven $\overline{Nu}/\overline{Nu}_0$ data series obtained with different Re but at a fixed Ro converges into a tight data trend in Figs. 7(a) and 7(b). This result confirms again that the Re impact on heat transfer can be isolated from the Ro and Bu effects by presenting the heat transfer results in terms of $\overline{Nu}/\overline{Nu}_0$. These ascending Bu driven Nusselt number ratios at fixed Ro reconfirm the improving Bu effect on heat transfer. But the slopes of these Bu driven Nusselt number ratios seen in Figs. 7(a) and 7(b) are systematically reduced as Ro increases. The improving Bu effect on \overline{Nu} is weakened as Ro increases. As the influences of Bu on \overline{Nu} vary with Ro , the interdependent Ro and Bu effect on \overline{Nu} is proven. The combined Ro and Bu effects could lead the leading $\overline{Nu}/\overline{Nu}_0$ to 0.78 at $Ro=0.15$, which requires design precautions. To uncouple the interdependent Ro and Bu effects, this research group has developed a method of parametric analysis that permits the generation of physically consistent \overline{Nu} correlations with the interdependent and isolated Re , Ro and Bu effects being determined [9-10, 17-18, 20-12]. However, as the laboratory test conditions are generally limited to operate the rotational heat transfer tests with the maximum T_w less than 200°C [1-21], the range of density ratio [$\Delta\rho/\rho=\beta(T_w-T_b)$] is less than the real engine conditions. The relatively small $\beta(T_w-T_b)$ range at each fixed Ro obtained at the laboratory scale experiments has usually led to the tight data band when $\overline{Nu}/\overline{Nu}_0$ are plotted against Bu . Fig. 7 is such an illustrative example. In view of the complete set of $\overline{Nu}/\overline{Nu}_0$ data presented, the compact $\overline{Nu}/\overline{Nu}_0$ correlation can be generated by using Bu as the controlling variable [15]. Justified by the data trends depicted in Figs. 7(a) and 7(b), the leading and trailing $\overline{Nu}/\overline{Nu}_0$ correlations are respectively generated as equations (8) and (9). The maximum discrepancy

between the experimental data and the correlation results obtained from equations (8) and (9) is less than $\pm 15\%$.

$$\frac{\overline{Nu}}{\overline{Nu}_0} = 1 - 1.95 \times Bu + 18.23 \times Bu^2 \quad \text{Leading (8)}$$

$$\frac{\overline{Nu}}{\overline{Nu}_0} = 1.18 - 0.188 \times e^{-57 \times Bu} + 0.756 \times Bu \quad \text{Trailing (9)}$$

f and η measurements

Figures 8(a)(c) and 8(b)(d) respectively plot the f and ff_∞ versus Re at fixed Ro and the f and ff_∞ versus Ro at fixed Re . The Re driven f variation at each test Ro for this parallelogram ribbed channel follows the typical exponential like decay, Fig. 8(a). It is worth noting that the pressure drops (ΔP) obtained from the stationary or rotating parallelogram ribbed channel at each test Ro still increase as Re increases. As f is defined as $[\Delta P / (0.5 \rho W_m^2)] \times (d/4L)$ which can be alternatively evaluated as $(\Delta P / Re^2) \times (\rho d^3 / 2\mu L)$, the Re exponent in the ΔP correlations for the present parallelogram ribbed channel at various Ro deem to be less than the Re exponent of 2 in the denominator of $\Delta P / Re^2$ for evaluating f . Due to the enhanced Coriolis secondary flows by increasing Ro , f increases as Ro increases at each fixed Re , Fig. 8(b).

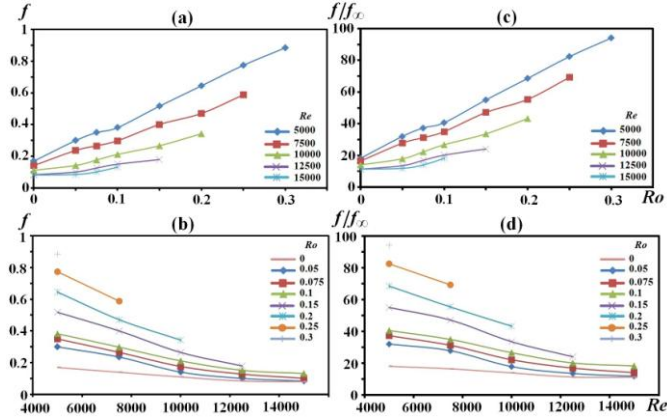


Fig. 8 (a)(c) f and ff_∞ versus Re at fixed Ro and (b)(d) f and ff_∞ versus Ro at fixed Re .

Having determined \overline{Nu} and f in the tested Ro and Re ranges of 0-0.3 and 5000-15000, the thermal performance factors (η) at various test conditions are evaluated as $(\overline{Nu} / Nu_\infty) / (ff_\infty)^{1/3}$ based on the same pumping power consumption. Fig. 9 depicts the variations of η against Re at the various Ro and Bu for this rotating channel. As f is obtained as the channel value, it is more relevant to present the thermal performance in terms of the averaged Nusselt number for leading and trailing walls. For the present parallelogram ribbed channel, both $\overline{Nu} / Nu_\infty$ and ff_∞ decrease as Re increases. Because such Re driven descending rate of $(ff_\infty)^{1/3}$ in the denominator of η is higher than the descending rate of $\overline{Nu} / Nu_\infty$ in the numerator of η , the thermal performance factors collected in Fig. 9 increase with the increase of Re . In view of the Ro impact on leading and trailing η , Fig. 9 generally shows the downward Ro driven data spread at each fixed Re , indicating the reduced η at the higher Ro . This result mainly reflects the data trend depicted by Fig. 8(d) in which ff_∞ increases as Ro increases. Because the Ro driven ascending rate of $(ff_\infty)^{1/3}$ in the denominator of η dominates the Ro driven η variation, the increase of Ro generally reduces η at each tested Re . There is also the Bu effect on η , which causes η to be increased with the increase of Bu due to the improving Bu effect on \overline{Nu} . A η review

indicates that the η factors are in the range of 0.979-1.575. As the thermal performance factors obtained from the present parallelogram ribbed channel are mostly above than unity, the skew ribs in the parallelogram channel are proven as an efficient HTE measure at the present test conditions.

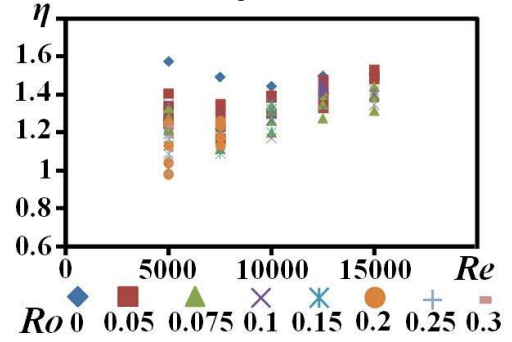


Fig. 9 η versus Re at tested Ro and Bu .

CONCLUSIONS

- As well as a reconfirmation, the near-wall flows acting with the sectional flows tripped by 45° ribs generate the attendant rib-wise obtuse-to-acute Nusselt number decays on the rib floor. The accelerated and separated flows caused by the abrupt blockage of the protruding rib produce the high Nusselt number bands along the rib tops. The shedding vortex triggered at the obtuse root behind each 45° rib serves as the dominant HTE mechanism between two successive 45° ribs by generating a midway skewed high Nu_0 stripe. As the length and width of such mid-way skewed Nusselt number stripe are respectively reduced and increased from those developed in the square and rectangular ribbed channels, the more rapid thermal and momentum diffusions in the parallelogram ribbed channel are generated, leading to the higher $\overline{Nu} / Nu_\infty$ from the rectangular counterparts as compared in [22]. The \overline{Nu}_0 correlation for the present parallelogram ribbed channel is generated as the function of Re .
- The distributing Nusselt number pattern on the rotating trailing wall generally follows the static result. But the distributions of Nusselt number over the rotating leading wall undergo considerable modifications by developing a haloed high Nusselt number zone aside the acute edge on the slanted entry corner due to the combined effect of Coriolis force and the flow twist at the immediate flow entrance. The Nusselt number imprint reflecting the shedding vortex behind the 45° rib on the rotating leading wall is diminished over the first three ribs; but recovered in a form to reflect the highly diffused vortex behind each 45° rib. Due to the high Nusselt number zone on the leading entry corner of the rotating parallelogram channel, the axial centerline leading Nu over the first three ribs are higher than the trailing and the stationary counterparts. The trailing centerline Nusselt numbers become consistently higher than the leading counterparts after the 2nd rib. As a typical Coriolis force effect, the trailing $\overline{Nu} / \overline{Nu}_0$ is consistently higher than its leading counterpart and above than unity, which increases as Ro increases. The leading $\overline{Nu} / \overline{Nu}_0$ is initially reduced from unity to 0.78 at Ro_{cr} of 0.15, above which $\overline{Nu} / \overline{Nu}_0$ turns to increase with the increase of Ro .

3. While the $\overline{Nu} / \overline{Nu}_0$ increases as Bu increases, the distributing Nu patterns over the leading and trailing ribbed walls remain similar as Bu varies. The leading and trailing $\overline{Nu} / \overline{Nu}_0$ correlations are successfully generated using Bu as the controlling variable.
4. The Re driven f variation at each test Ro for the stationary and rotating parallelogram ribbed channel follows the typical exponential like decay. Due to the enhanced Coriolis secondary flows by increasing Ro , f increases with the increase of Ro at each fixed Re .
5. The thermal performance factor (η) increases with the increase of Re or Bu but generally decreases with the increase of Ro . Leading and trailing $\overline{Nu} / \overline{Nu}_\infty$ are in the respective ranges of 2.97-5.05 and 3.52-5.65. As the η factors obtained from the rotating parallelogram ribbed channel are mostly above than unity, the skew ribs on two opposite leading and trailing walls of a rotating parallelogram channel appear as an effective and efficient HTE measure for promoting the internal cooling performance of a gas turbine rotor blade.

ACKNOWLEDGEMENT

The research facilities are sponsored by the grant NSC 97-2221-E-022-013-MY3 from National Science Council, Taiwan.

REFERENCES

- [1] L. Al-Hadhrami, J.-C. Han, 2002, Effect of rotation on heat transfer in two-pass square channels with five different orientations of 45° angled rib turbulators, *Int. J. Heat Mass Transfer*, 46, 653-669.
- [2] T.-M. Liou, S.W. Chang, J.H. Hung, S.F. Chiou, 2007, High rotation number heat transfer of a 45-deg rib-roughened rectangular duct with two channel orientations, *Int. J. Heat Mass Transfer*, 50, 4063-4078.
- [3] S.P. Harasgama, W.D. Morris, 1988, The influence of rotation on the heat transfer characteristics of circular, triangular and square-sectioned coolant passages of gas turbine rotor blades, *ASME J. Turbomachinery*, 110, 44-50.
- [4] S.W. Chang, W.D. Morris, 1998, A Comparative study of heat transfer between rotating circular smooth-walled and square rib-roughened ducts with cooling application for gas turbine rotor blades, *JSME Int. J. Series B*, 41, 302-315.
- [5] R.J. Clifford, W.D. Morris, S.P. Harasgama, 1984, An experimental study of local and mean heat transfer in a triangular sectioned duct rotating in the orthogonal mode, *ASME J. Engineering for Gas Turbines and Power*, 106, 661-667.
- [6] S. Dutta, J.-C. Han, C.P. Lee, 1996, Local heat transfer in a rotating two-pass ribbed triangular duct with two model orientations, *Int. J. Heat Mass Transfer* 39, 707-715.
- [7] B.V. Johnson, J.H. Wagner, G.D. Steuber, F.C. Yeh, 1994, Heat transfer in rotating serpentine passages with trip skewed to the flow, *ASME J. Turbomachinery*, 116, 113-123.
- [8] H. Iacovides, D.C. Jackson, G. Kelemenis, B.E. Launder, Y.-M. Yuan, 2001, Flow and heat transfer in a rotating U-bend with 45° ribs, *Int. J. Heat Fluid Flow* 22, 308-314.
- [9] S.W. Chang and W.D. Morris, 2003, Heat transfer in a radially square duct fitted with in-line transverse ribs, *Int. J. Thermal Sciences* 42, 267-282.
- [10] S.W. Chang, T.-M. Liou, W.-H. Yeh, J.-H. Hung, 2007, Heat transfer in a radially rotating square-sectioned duct with two opposite walls roughened by 45 degree staggered ribs at high rotation numbers, *ASME J. Heat Transfer*, 129, 188-199.
- [11] C.Y. Soong, S.T. Lin, G.J. Hwang, 1991, An experimental study of convective heat transfer in radially rotating rectangular ducts, *ASME J. Heat Transfer*, 113, 604-611.
- [12] T.S. Griffith, L. Al-Hadhrami, J.-C. Han, 2003, Heat transfer in rotating rectangular cooling channels (AR=4) with dimples, *ASME J. Turbomachinery* 125, 555-563.
- [13] A. Murata and S. Mochizuki, 2003, Effect of cross-sectioned aspect ratio on turbulent heat transfer in an orthogonally rotating rectangular duct with angled rib turbulators, *Int. J. Heat Mass Transfer*, 46, 3119-3133.
- [14] G. Su, H.C. Chen, J.-C. Han, J.D. Heidmann, 2004, Computation of flow and heat transfer in rotating two-pass rectangular channels (AR = 1:1, 1:2, and 1:4) with smooth walls by a Reynolds stress turbulence model, *Int. J. Heat Mass Transfer*, 47, 5665-5683.
- [15] M. Huh, Y.-H. Liu, J.-C. Han, 2009, Effect of rib height on heat transfer in a two pass rectangular channel (AR=1:4) with a sharp entrance at high rotation numbers, *Int. J. Heat Mass Transfer* 52, 4635-4649.
- [16] T.-M. Liou, S.W. Chang, J.S. Chen, T.L. Yang, Y.-A. Lan, 2009, Influence of channel aspect ratio on heat transfer in rotating rectangular ducts with skewed ribs at high rotation numbers, *Int. J. Heat Mass Transfer*, 52, 5309-5322.
- [17] S.W. Chang, T.L. Yang, T.-M. Liou, G.F. Hong, 2009, Heat transfer in rotating scale-roughened trapezoidal duct at high rotation numbers, *J. Applied Thermal Engineering* 29, 1682-1693.
- [18] S.W. Chang, T.-M. Liou, S.F. Chiou, S.F. Chang, 2008, Heat transfer in high-speed rotating trapezoidal duct with rib-roughened surfaces and air bleeds from the wall on apical side, *ASME J. Heat Transfer*, 130, 061702-1~061702-13.
- [19] K.M. Kim, Y.Y. Kim, D.H. Lee, D.H. Rhee, H.H. Cho, 2007, Influence of duct aspect ratio on heat/mass transfer in coolant passages with rotation, *Int. J. Heat Fluid Flow*, 28, 357-373.
- [20] S.W. Chang, T.-M. Liou, Y. Po., 2010, Coriolis and rotating buoyancy effect on detailed heat transfer distributions in a two-pass square channel roughened by 45° ribs at high rotation numbers, *Int. J. Heat Mass Transfer*, 53, 1349-1363.
- [21] S.W. Chang, A. W. Lees, T.-M. Liou, G.F. Hong, 2010, Heat transfer of a radially rotating furrowed channel with two opposite skewed sinusoidal wavy walls, *Int. J. Thermal Sciences*, 49, 769-785.
- [22] P.A. Matthews, 2009, An experimental study of heat transfer in the cooling channels of gas turbine blades, M.Ph., Swansea University.
- [23] J.A.J. Khamaj, 2002, An experimental study of heat transfer in the cooling channels of gas turbine rotor blades, Ph.D. thesis, University of Wales, Swansea.
- [24] Editorial Board of ASME Journal of Heat Transfer, 1993, Journal of heat transfer policy on reporting uncertainties in experimental measurements and results, *ASME Journal of Heat Transfer* 115, 5-6.